High-resolution bispectral imager at 1000 frames per second

Marija Strojnik[1,*] and Gonzalo Paez[2]

[1]*Centro de Investigaciones en Optica, Apdo. Postal 1-948, C.P. 37000, Leon, Guanajuato, Mexico*
[2]*gpaez@cio.mx*
**mstrojnikp@aol.com*

Abstract: We describe a bispectral, 1000-frames per second imaging instrument working simultaneously in two spectral bands. These bands may be selected for a specific application; however, we implement a pair centered at 4.3 μm and 4.66 μm. Synchronization is accomplished by employing a single focal plane array. To demonstrate the performance of the bispectral imager, we apply it to the methane flame of a Bunsen burner in a near conjugate configuration with flame image length subtending at about 200 pixels. The instrument detects bispectral puffing at 2 Hz, pulsations, and bispectral radiation oscillations, first reported here in two spectral intervals. The period of oscillatory spectral components in two bands is the same, about 3 Hz for this flame, with delay of a quarter period between them, first reported here. With 1-ms integration time, we detect significant formation of turbulence and vortices, especially pronounced in the region where the flame transitions into a plume. We display bispectral ratioed images of flames in near-real time with either the laboratory or the field device.

OCIS codes: (170.0110) Imaging systems; (230.1360) Beam splitters; (260.3060) Infrared; (200.3050) Information processing; (280.1740) Combustion diagnostics; (300.6340) Spectroscopy, infrared.

References and links

1. P. Kauranen, S. Andersson-Engels, and S. Svanberg, "Spatial mapping of flame radical emission using a spectroscopic multi-colour imaging system," Appl. Phys. B **53**(4), 260–264 (1991).
2. H. Jiang, Y. Qian, and K. T. Rhee, "High-speed dual-spectra infrared imaging," Optim. Eng. **32**(6), 1281–1289 (1993).
3. P. M. Brisley, G. Lu, Y. Yan, and S. Cornwell, "Three-dimensional temperature measurement of combustion flames using a single monochromatic CCD camera," IEEE Trans. Instrum. Meas. **54**(4), 1417–1421 (2005).
4. L. A. Kranendonk, X. An, A. W. Caswell, R. E. Herold, S. T. Sanders, R. Huber, J. G. Fujimoto, Y. Okura, and Y. Urata, "High speed engine gas thermometry by Fourier-domain mode-locked laser absorption spectroscopy," Opt. Express **15**(23), 15115–15128 (2007).
5. P. Wright, N. Terzija, J. L. Davidson, S. Garcia-Castillo, C. Garcia-Stewart, S. Pegrum, S. Colbourne, P. Turner, S. D. Crossley, T. Litt, S. Murray, K. B. Ozanyan, and H. McCann, "High-speed chemical species tomography in a multi-cylinder automotive engine," Chem. Eng. J. **158**(1), 2–10 (2010).
6. B. A. Rankin, D. L. Blunck, and J. P. Gore, "Infrared imaging and spatiotemporal radiation properties of a turbulent nonpremixed jet flame and plume," J. Heat Transfer **135**(2), 021201 (2012).
7. J. L. Harley, B. A. Rankin, D. L. Blunck, J. P. Gore, and K. C. Gross, "Imaging Fourier-transform spectrometer measurements of a turbulent nonpremixed jet flame," Opt. Lett. **39**(8), 2350–2353 (2014).
8. M. Strojnik, G. Paez, and M. K. Scholl, "Combustion initiation and evolution during the first 400 msec in a gas burner at 10 μm," Infrared Phys. Technol. **61**, 42–49 (2013).
9. D. Blunck, S. Basu, Y. Zheng, V. Katta, and J. Gore, "Simultaneous water vapor concentration and temperature measurements in unsteady hydrogen flames," Proc. Combust. Inst. **32**(2), 2527–2534 (2009).
10. K. Biswas, Y. Zheng, C. H. Kim, and J. Gore, "Stochastic time series analysis of pulsating buoyant pool fires," Proc. Combust. Inst. **31**(2), 2581–2588 (2007).
11. T. Werblinski, S. R. Engel, R. Engelbrecht, L. Zigan, and S. Will, "Temperature and multi-species measurements by supercontinuum absorption spectroscopy for IC engine applications," Opt. Express **21**(11), 13656–13667 (2013).

#243169 Received 19 Jun 2015; revised 27 Jul 2015; accepted 29 Jul 2015; published 1 Sep 2015

12. S. Roy, P. J. Kinnius, R. P. Lucht, and J. R. Gord, "Temperature measurements in reacting flows by time resolved femtosecond coherent anti-Stokes Raman scattering (fs-CARS) spectroscopy," Opt. Commun. **281**(2), 319–325 (2008).
13. M. P. Arroyo and R. K. Hanson, "Absorption measurements of water-vapor concentration, temperature, and line-shape parameters using a tunable InGaAsP diode laser," Appl. Opt. **32**(30), 6104–6116 (1993).
14. L. Ma and W. Cai, "Numerical investigation of hyperspectral tomography for simultaneous temperature and concentration imaging," Appl. Opt. **47**(21), 3751–3759 (2008).
15. T. R. Meyer, S. Roy, T. N. Anderson, J. D. Miller, V. R. Katta, R. P. Lucht, and J. R. Gord, "Measurements of OH mole fraction and temperature up to 20 kHz by using a diode-laser-based UV absorption sensor," Appl. Opt. **44**(31), 6729–6740 (2005).
16. X. An, A. W. Caswell, J. J. Lipor, and S. T. Sanders, "Optimized wavelength selection for molecular absorption thermometry," Appl. Spectrosc. **69**(4), 464–472 (2015).
17. L. A. Kranendonk, A. W. Caswell, and S. T. Sanders, "Robust method for calculating temperature, pressure, and absorber mole fraction from broadband spectra," Appl. Opt. **46**(19), 4117–4124 (2007).
18. L. S. Rothman, C. P. Rinsland, A. Goldman, S. T. Massie, D. P. Edwards, J.-M. Flaud, A. Perrin, C. Camy-Peyret, V. Dana, J.-Y. Mandin, J. Schroeder, A. Mccann, R. R. Gamache, R. B. Wattson, K. Yoshino, K. V. Chance, K. W. Jucks, L. R. Brown, V. Nemtchinov, and P. Varanasi, "The HITRAN molecular spectroscopic database and HAWKS (HITRAN atmospheric workstation): 1996 edition," J. Quant. Spectrosc. Radiat. Transf. **60**(5), 665–710 (1998).
19. L. S. Rothman, I. E. Gordon, R. J. Barber, H. Dothe, R. R. Gamache, A. Goldman, V. I. Perevalov, S. A. Tashkun, and J. Tennyson, "HITEMP, the high-temperature molecular spectroscopic database," J. Quant. Spectrosc. Radiat. Transf. **111**(15), 2139–2150 (2010).
20. S. A. Tashkun and V. I. Perevalov, "CDSD-4000: high-resolution, high-temperature carbon dioxide spectroscopic databank," J. Quant. Spectrosc. Radiat. Transf. **112**(9), 1403–1410 (2011).
21. S. Depraz, M. Y. Perrin, P. Riviere, and A. Soufiani, "Infrared emission spectroscopy of CO2 at high temperature. Part II: Experimental results and comparisons with spectroscopic databases," J. Quant. Spectrosc. Radiat. Transf. **113**(1), 14–25 (2012).
22. S. Depraz, M. Y. Perrin, P. Riviere, and A. Soufiani, "Infrared emission spectroscopy of CO2 at high temperature. Part I: Experimental setup and source characterization," J. Quant. Spectrosc. Radiat. Transf. **113**(1), 1–13 (2012).
23. P. R. Solomon, P. E. Best, R. M. Carangelo, J. R. Markham, P.-L. Chien, R. J. Santoro, and H. G. Semerjian, "FT-IR emission/transmission spectroscopy for in situ combustion diagnostics," Proc. Combust. Inst. **21**(1), 1763–1771 (1988).
24. P. E. Best, P. L. Chien, R. M. Carangelo, P. R. Solomon, M. Danchak, and I. Ilovici, "Tomographic reconstruction of FT-IR emission and transmission spectra in a sooting laminar diffusion flame: species concentrations and temperatures," Combust. Flame **85**(3–4), 309–318 (1991).
25. M. R. Rhoby, D. L. Blunck, and K. C. Gross, "Mid-IR hyperspectral imaging of laminar flames for 2-D scalar values," Opt. Express **22**(18), 21600–21617 (2014).
26. H. M. Hertz, "Experimental-determination of 2-D flame temperature-fields by interferometric tomography," Opt. Commun. **54**(3), 131–136 (1985).
27. K. B. Chung, F. C. Gouldin, and G. J. Wolga, "Experimental reconstruction of the spatial density distribution of a nonreacting flow with a small number of absorption measurements," Appl. Opt. **34**(24), 5492–5500 (1995).
28. P. Wright, C. A. Garcia-Stewart, S. J. Carey, F. P. Hindle, S. H. Pegrum, S. M. Colbourne, P. J. Turner, W. J. Hurr, T. J. Litt, S. C. Murray, S. D. Crossley, K. B. Ozanyan, and H. McCann, "Toward in-cylinder absorption tomography in a production engine," Appl. Opt. **44**(31), 6578–6592 (2005).
29. L. Ma, W. Cai, A. W. Caswell, T. Kraetschmer, S. T. Sanders, S. Roy, and J. R. Gord, "Tomographic imaging of temperature and chemical species based on hyperspectral absorption spectroscopy," Opt. Express **17**(10), 8602–8613 (2009).
30. J. Hult, R. S. Watt, and C. F. Kaminski, "High bandwidth absorption spectroscopy with a dispersed supercontinuum source," Opt. Express **15**(18), 11385–11395 (2007).
31. J. M. Langridge, T. Laurila, R. S. Watt, R. L. Jones, C. F. Kaminski, and J. Hult, "Cavity enhanced absorption spectroscopy of multiple trace gas species using a supercontinuum radiation source," Opt. Express **16**(14), 10178–10188 (2008).
32. T. Kraetschmer, D. Dagel, and S. T. Sanders, "Simple multiwavelength time-division multiplexed light source for sensing applications," Opt. Lett. **33**(7), 738–740 (2008).
33. J. H. Kim, M.-K. Chen, C.-E. Yang, J. Lee, K. Shi, Z. Liu, S. S. Yin, K. Reichard, P. Ruffin, E. Edwards, C. Brantley, and C. Luo, "Broadband supercontinuum generation covering UV to mid-IR region by using three pumping sources in single crystal sapphire fiber," Opt. Express **16**(19), 14792–14800 (2008).
34. Y. Sych, R. Engelbrecht, B. Schmauss, D. Kozlov, T. Seeger, and A. Leipertz, "Broadband time-domain absorption spectroscopy with a ns-pulse supercontinuum source," Opt. Express **18**(22), 22762–22771 (2010).
35. J. Geng, Q. Wang, and S. Jiang, "High-spectral-flatness mid-infrared supercontinuum generated from a Tm-doped fiber amplifier," Appl. Opt. **51**(7), 834–840 (2012).
36. W. R. Ashby, "Principles of the self-organizing system," in *Principles of Self-Organization: Transactions of the University of Illinois Symposium*, H. Von Foerster and G. W. Zopf, Pergamon Press (United Kingdom, 1962).

#243169 Received 19 Jun 2015; revised 27 Jul 2015; accepted 29 Jul 2015; published 1 Sep 2015

37. M. Strojnik and G. Paez, "Radiometry," in *Handbook of Optical Engineering*, D. Malacara, B. Thompson, Marcel Dekker (New York, 2001).
38. J. Castrellon, G. Paez, and M. Strojnik, "Remote temperature sensor employing erbium-doped silica fiber," Infrared Phys. Technol. **43**(3-5), 219–222 (2002).
39. M. Strojnik and G. Paez, "Spectral dependence of absorption sensitivity on concentration of oxygenated hemoglobin: pulse oximetry implications," J. Biomed. Opt. **18**(10), 108001 (2013).
40. M. Strojnik and G. Paez, "Optical system for bispectral Imaging in mid-IR at 1000 frames per second," Adv. Opt. Technol. **2013**, 905870 (2013).
41. M. S. Scholl and J. W. Scholl, "Time and position varying infrared scene simulation," in Infrared Technology XIII, Proc. SPIE **819**, 297–301 (1987).
42. J. W. Scholl and M. S. Scholl, "Measurement of small temperature fluctuations at high average temperature," in Infrared Technology XIV, Proc. SPIE **972**, 409–415 (1988).

1. Introduction

The nature of combustion dynamics and evolution has only recently started to be investigated. Previously, this research was hindered by rapidity of this spatially resolved process. With recent semiconductor and IR detector technology development, instruments started evolving with the required spatial resolution, temporal bandwidth, memory, and software capabilities. Four spectral images of the flame are obtained over the same image space with aperture-multiplexing, using four filters inserted into entrance aperture, in the visible spectral interval [1]. An additional aperture implements sequential imaging in each spectral band.

An early experimental setup to image a flame in two spectral intervals incorporates two cameras with 60 by 60 pixels and a beam splitter for beam combining [2]. An operator performs visual alignment of two images upon inspection on two monitors. Two separate static spectral images of hydrogen flame in 2.2 – 2.5 μm and 4.5 – 5.5 μm spectral intervals are presented, in two gray levels (black and white in the on-line rendition). This allows the authors to report on determination of 2-D temperature and water concentration. With a reported system capability of processing at 10 MHz rate and 12 bits depth, 500 frames per second (fps) are presented in two gray levels. Reportedly, the challenges of this work are in electronics: control of the start of imaging; triggering of the imaging of individual frames; and compilation, storage, and readout of a preset number of images in each measurement cycle. The low resolution imaging and lost frames indicate the bandwidth cost of two cameras and electronics for their synchronization.

Two-color thermometry is used to reconstruct the flame and to determine its temperature distribution, assuming rotational symmetry in the structure of the flame, recorded with a CCD camera [3].

High-temperature and highly-temporally variant processes take place in closed volume (automotive [4,5]), moving environments (aerospace [6,7]), with localized heat generation (industrial and domestic applications [8]), and in unpredictable conditions (wild and/or accidental fires [9]). Non-contact, non-invasive, radiative-emission- and absorption- based techniques are preferably implemented due to the existence of enormous temperature gradients and temporal evolution in the combustion space [10,11]. In the time-resolved femtosecond coherent anti-Stokes Raman scattering (fs-CARS) spectroscopy the transition time is temperature dependent [12]. High bandwidth of the detection system is required for a single temperature measurement.

The experimental procedures to determine temperature measure absorption from a single line of a combustion species (CO_2 [carbon dioxide], OH [hydroxide], or H_2O [water] and $NO_{x)}$ [13–16]. Temperature distribution is derived upon measuring the emission or absorption through a column, employing catalogues of the spectra measured in laboratory conditions [17–22]. Multiple line-of-sight Fourier-transform spectrometer infrared (FTSIR) measurements, when paired with appropriate tomographic deconvolution algorithms, can be used to simultaneously determine temperature and mole fractions of major flame species [23, 24]. Measurements are performed consecutively at several positions along the length of the

#243169 Received 19 Jun 2015; revised 27 Jul 2015; accepted 29 Jul 2015; published 1 Sep 2015

flame. This technique evolved into imaging FTIR with the development of two-dimensional focal plane technology (FPT) over the last three decades [25].

Three-dimensional reconstruction of flame temperature is still in early development. The technology needs to overcome challenges of integration of the number of probe laser beams required, the need for measurement of fine spatial and temporal details, and the velocity of combustion processes. Significant progress has been reported for stationary and rotationally symmetric combustion fields [26–29].

Another implementation of absorption spectroscopy takes advantage of supercontinuum lasers to rapidly sample a number of spectral lines in succession, also requiring high bandwidth detection systems [30–35].

Here we report on the development and demonstration of feasibility of a high temporal-resolution bispectral imaging technique. We designed and built an instrument to simultaneously obtain two images of the same scene with the capability to filter them independently, at 1000 fps. We apply it to a combustion whose initiation, establishment, formation and maintenance collectively are an example of a complex, chaotic system [36]. Specifically, in this work we discuss: 1. Theoretical basis for two spectral-band imaging and ratioing; 2. Relative calibration of two channels; 3. Side-by-side simultaneous imaging in two spectral bands to obtain incidance (power in a spectral band per pixel [37]) at 1000 fps; 4. Determination of 2-D spectral ratio; 5. Performance demonstration of 2-D high speed bispectral imager upon detection of pulsing, puffing, and oscillations in two spectral intervals in combustion; and 6. Identification of significant spatio-temporal features, low- and high ratio pixel ensembles traveling through the combustion volume simultaneously.

2. Spectral ratio imaging

The high-speed bispectral imager samples rapidly-evolving spatially-resolved processes every 1 ms. An example of such a dynamic process is combustion initiation, sustainability and maintenance in domestic applications and wild fires. We previously determined that the flame evolves in a causally-comprehensible and fluid manner when sampled at 1 ms intervals in the visible and IR [8]. We treat it as a complex system and make no additional assumptions.

We monitor radiation in two spectral bands. We chose two, because this is the most efficient number for a multiple band instrument, in terms of instrument hardware and software, and is a sufficient number as a proof of concept. Finally, it is the number of spectral bands used in the *ratioing* methods, employed when the absolute calibration is not possible or critical for the validity of measurement. Ratioing methods are often used in fiber optic sensors [38] and always in blood oxymetry [39].

The 2-D ratio is then defined as emission in the band that always generates radiation, band 1, over the sum of emissions in both bands, to minimize errors arising from noise. This spatially and temporally resolved ratio distribution $R_{1,2}(x,y,t)$ is a number between 0 and 1 for each pixel. It is equal to 1 when the emission exists only in band 1; it decreases monotonically toward zero with increasing amount of radiation in band 2.

$$R_{1,2}(x,y,t) = \frac{L_{\Delta\lambda 1}(x,y,t)}{L_{\Delta\lambda 1}(x,y,t) + L_{\Delta\lambda 2}(x,y,t)} \tag{1}$$

Here, $L_{\Delta\lambda i}$ denotes radiance [W/(m^2 sr)] in bands i, i = 1,2. The two spectral bands are often chosen according to the key emissions produced in monitored processes.

2.1 Bi-spectral IR imaging

Next we describe implementation of the laboratory device forming two simultaneous images in two spectral bands at 1000 fps. High resolution, low distortion optical imaging system projects two images side by side on the central part of the focal plane array (FPA), using two channels [40]. The most significant optical design requirement is that the image of projected

#243169 Received 19 Jun 2015; revised 27 Jul 2015; accepted 29 Jul 2015; published 1 Sep 2015

pixel in the object space be formed over the corresponding pixels with more than 95% geometrical fidelity with each channel. For the points on the object plane, the distortion is actually less than 0.5%. It increases for flame volume outside the object plane.

2.2 Experimental setup

The schematic of the experimental setup is presented in Fig. 1. The specimen, object of interest, or flame for performance demonstration, is placed on the left side of the compact optical assembly. The 50/50 IR power-dividing beam splitter transmits 50% of the collected radiation and reflects the other 50%.

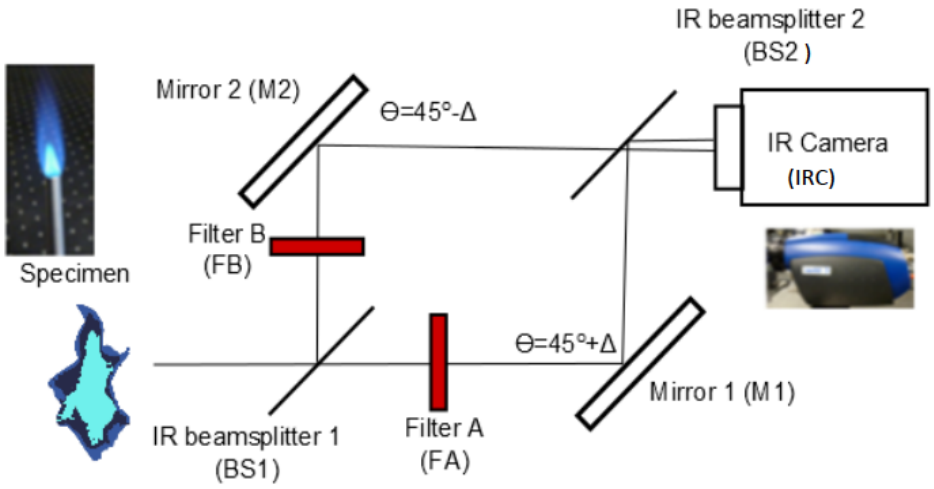

Fig. 1. Schematic layout of a bispectral experiment with simultaneous imaging in two parallel channels. Images are displaced side-by-side by aligning mirrors at 45° +/– Δ. Images are captured by the high-resolution FPA employing InSb. For bispectral flame imaging, radiation is filtered with filters FA and FB centered at 4.3 μm and at 4.66 μm.

Mirrors M1 and M2 are placed at angles of 45+/–Δ degrees, respectively. This mirror orientation assures that two images in the focal plane are physically separated (to be contrasted with [1]). Fine alignment with a test target may be performed prior to the actual measurement to verify that there is no image overlap in IR. Mirrors M1 and M2 are gold-coated mirrors. The system is symmetrical: a more complex optical architecture may be implemented to form four images, using the horizontal and the vertical planes.

We insert two custom-designed spectral filters in two otherwise identical paths to obtain two adjacent spectral images through two spectral channels. On each frame, the *left* image is filtered using a 4.66-μm centered filter B [0.164-μm full width at half maximum (FWHM) transmission]. The *right* flame is filtered with a 4.3-μm centered filter A (0.181-μm FWHM band). These two filters were chosen upon expected flame IR signature. Other filters may be chosen for monitoring other wavelength bands in other processes. BS1IR and BS2IR are mid-wave IR (MWIR) 50/50 beam-splitters.

Two images are incident on and detected by the indium antimonide (InSb) FPA. We integrate an IR camera with a sensitivity of 15 mK, responsive over a spectral range from 3 μm to 5 μm, with 14 bits dynamic range, full radiometric capabilities, and integration time from 10 μs to 5000 μs (frame rate of from 400 fps at full frame up to 20,000 fps in subframing mode, in contrast with [2]). The radiation carrying useful information from the flame is incident on and detected by the central part of the InSb detector array in our setup, taking advantage of the flame aspect ratio.

#243169 Received 19 Jun 2015; revised 27 Jul 2015; accepted 29 Jul 2015; published 1 Sep 2015

2.3 Experimental setup and field instrument

The bispectral imager is designed for compactness. We built a laboratory prototype and a robust field device for use in uncontrolled field conditions. Photographs of both with the covers removed are presented in Fig. 2.

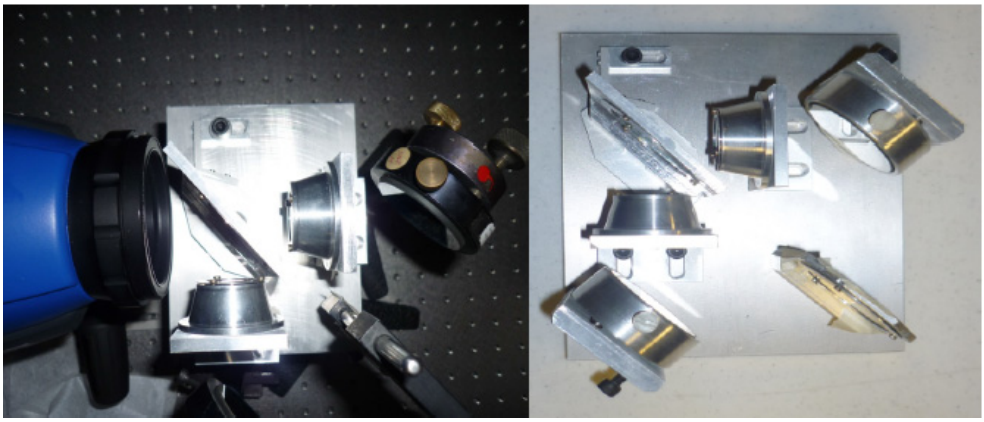

Fig. 2. Photographs of the experimental setup and the field bispectral imager, with the cover removed. The IR camera is included in the photo of the laboratory arrangement.

3. Calibration

The physical lengths along both channels are the same, so radiation emitted from a single pixel projected on the object plane arrives simultaneously on the corresponding two pixels in the FPA. The images are recorded on the same FPA; therefore, neither synchronization nor responsivity calibration is required.

The correspondence between pixels of two images in the focal plane is established upon spatial and radiometric calibration. It is stored in the transformation matrix.

3.1 Spatial calibration

In the past, ratioing techniques have used all detected radiation at specific spectral bands, resulting in the ratio determination as a division of two numbers. For high-spatial resolution ratioing, pixel co-registration in images is critical to ensure radiation originates at the same projected object pixel. This requires that a precise spatial relationship between two image pixels arising from one object pixel be established.

This challenge may be appreciated with the aid of Fig. 3 where the left image is produced by radiation in band 2 (4.66 μm) and the right image by radiation in band 1 at (4.3 μm). We see that the amount of radiation detected through band 2 is appreciably smaller than that through band 1. Also, the spatial extent of the band 2 image is significantly smaller than that of band 1. The most memorable difference is observed in the radiative tail raising above the flame in band 1 (4.3 μm); the corresponding pixels in band 2 cannot be identified.

After the bispectral images are positioned approximately on the focal plane, their spatial relationship is established by performing relative calibration. The spectral filters FA and FB are removed from their respective arms. In Fig. 4, we show two images of a single object – a butane flame – through two channels without filters in the 3 – 5 μm interval. Two nearly identical images are obtained in the focal plane.

#243169 Received 19 Jun 2015; revised 27 Jul 2015; accepted 29 Jul 2015; published 1 Sep 2015

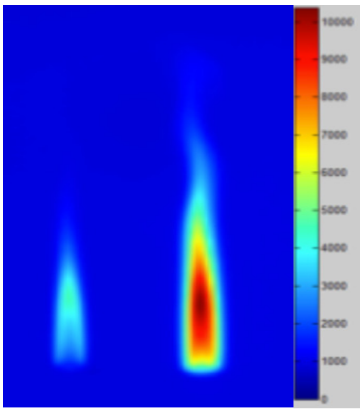

Fig. 3. The FPA of the bispectral imager detects two spectral images every ms. Flame images are obtained in spectral bands at 4.66 μm (band 2, left) and 4.3 μm (band 1, right).

In most optical and infrared instruments, there are some minute differences for radiation detected by the nominally identical channels. Flame images in the right portion of Fig. 4 appear nearly identical to the naked eye. Subtle differences in shape and background include the radially-dependent field aberrations and field-illumination falloff. In IR, we observe narcissus, a bright annulus in a background, and some ghost images on the lower right side of each flame image.

We perform geometrical correction (magnification and stretching) in such a way that there is a perfect overlap between each pair of image points. A transformation matrix is constructed by relating image of projected object pixel (j,k) in spectral interval $\Delta\lambda_1$ with that in spectral interval $\Delta\lambda_2$. This transformation is encoded into a spatial calibration matrix. Calibration data processing steps are standard for a look-up-table pixel-wise calibration.

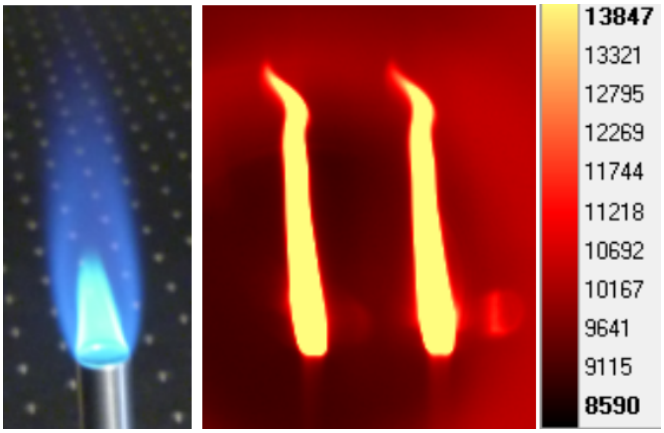

Fig. 4. Spatial calibration. Two images (right) of a single test object (left) are simultaneously captured through different optical channels after removing spectral filters.

3.2 Radiometric calibration

There are several approaches to calibration of the detected radiation in two images. For this proof of concept demonstration of a ratioing technique, it is not necessary to perform a complex radiometric calibration, but rather to complete the removal of inherent noise and background radiation. In this IR interval, removal of background is quite challenging.

Radiometric calibration is not necessary in bispectral measurements because we are interested in determining relative rather than absolute IR radiant power. We use a target of known, uniform temperature distribution with well characterized emissivity. The measured

#243169 Received 19 Jun 2015; revised 27 Jul 2015; accepted 29 Jul 2015; published 1 Sep 2015

pixel response through each channel without filters to a uniform source provides the (non)uniformity response. The calibration of each pair of image pixels gives us a radiometric correction matrix. Together with the geometrical correction, the radiometric correction matrix forms a transformation matrix. Its application to the image in band 1 represents calibration. The relative calibration assures accurate bispectral ratioed imaging of unknown objects.

We additionally use a blackbody radiation reference source, as customary in accurate absolute radiation measurements [41,42] to confirm the accuracy of absolute measurements.

We calculate ratio for each object projected-pixel in each frame, according to Eq. (1). It is presented in Fig. 5 for spectral images of Fig. 3. The value of each pixel is calculated as $c_2/(c_1 + c_2)$, where c_i denotes the number of counts in spectral bands i = 1 and 2. Color range for the ratio on the right is coded dark blue for near 0 values to dark red for ratios approaching 1. We may display the 2-D ratio for a few key times or present its evolution as a function of time. For presentation to the human visual system, the playback has to be slowed down to 40 to 80 fps or interlaced (time dilation by a factor of about 20), depending on the rapidity of changes in scene.

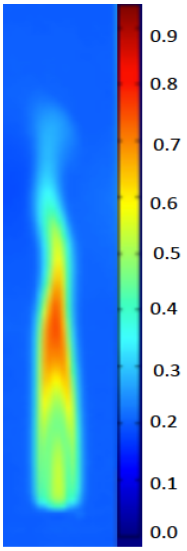

Fig. 5. A single bispectral ratioed image.

4. Results

We study a butane flame generated by a Bunsen burner as an illustration of the high temporal and high spatial resolution of the instrument. It may burn LPG (propane to butane in a ratio of 60% to 40%) or a natural gas (methane > 90%). We show a sequence of two-dimensional bispectral ratio images in Fig. 6, measured every millisecond but displayed only every 83 ms. Figure 6 presents twelve bispectral images of a butane flame during the initial second, generated under low- (left) and high- (right) oxygenation conditions.

The images are captured, processed, and displayed at the rate of 1,000 frame per second; however, some of the significant features exhibited in 2-D frames may be appreciated with just a few representative images. The vertical bar in the middle codes the color scale: dark blue represents ratios close to 0, denoting a strong presence of radiation in band 2; dark red indicates ratios close to 1, signaling weak radiation in band 2.

#243169 Received 19 Jun 2015; revised 27 Jul 2015; accepted 29 Jul 2015; published 1 Sep 2015

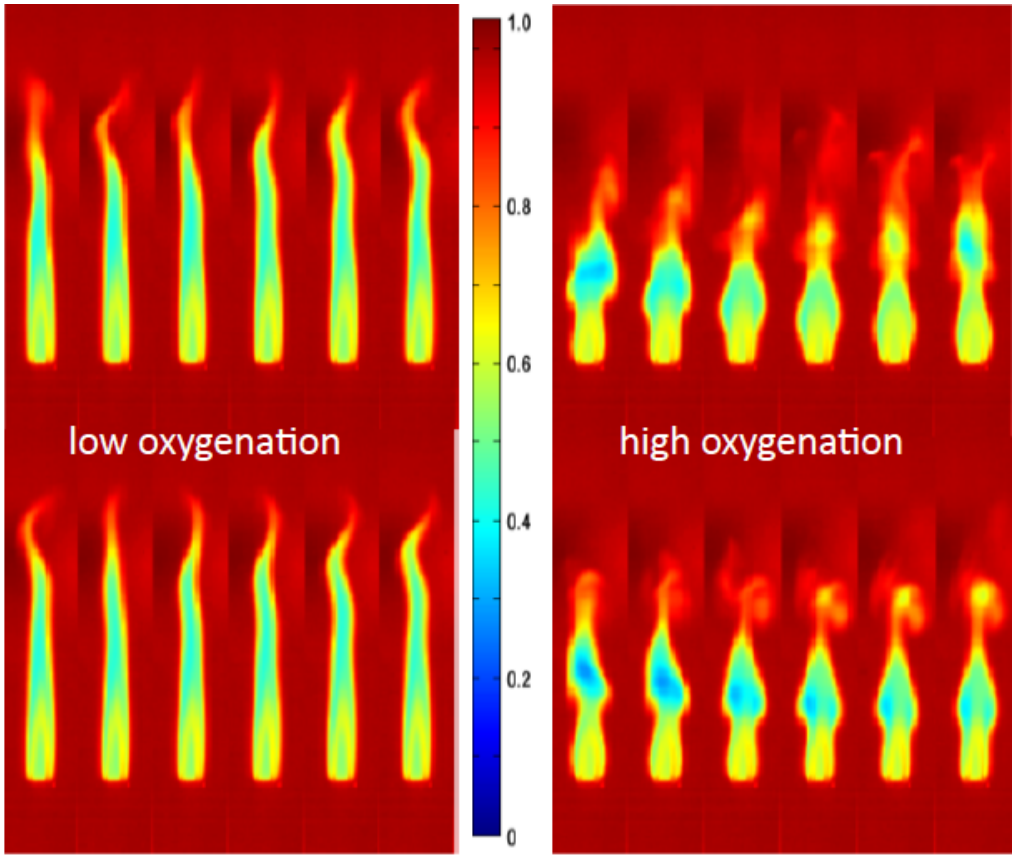

Fig. 6. Twelve representative images illustrate the bispectral ratio images at t = 83 ms (top left image) to t = 1 s (bottom right image), separated by Δt = 83 ms. Left panel presents the case of low oxygenation, right panel that of high oxygenation. The color scale is indicated in the middle with 0 (dark blue) denoting low values for the ratio and 1 (dark red) indicating high values.

Examining the low-oxygenation case, we identify several features in its temporal evolution. First, the bright primary flame is present in all displayed frames with about equal radiative contribution from both spectral intervals. Second, the combustion volume is similar in shape to the long diffusion flames, indicating mostly laminar flow through the flame region. The flame terminates in a somewhat random flame turbulence at flame-plume transition region. Third, the ratio is above 0.6 in the first one-third of the flame length where the oxygen is supplied to the fuel. This means that the first spectral band contributes more radiation to the ratio in the first one third of the flame. In the next half-length of the flame, the oxygen has been depleted to a large degree and the ratio is decreased to about 0.5. The ratio is again increased in the last segment of the flame where the oxygen from the surrounding atmosphere is drawn into the combustion volume. In this last segment, the by-products are also expelled with a degree of turbulence. The remaining fuel is combined with oxygen from the surrounding area, to produce imaging primarily in the first band, with a relative ratio increasing to 0.9.

The high oxygenation case illustrates much more interesting processes, exhibiting several remarkable temporal features. First, the combustion volume is more compact for a high-oxygenation flame. We observe that the flame forms a neck and a bulge above it with an oscillation frequency of about 2 Hz. The distribution of radiation represented by the ratio images presents puffing and oscillation as a function of time. The region of low ratio

#243169 Received 19 Jun 2015; revised 27 Jul 2015; accepted 29 Jul 2015; published 1 Sep 2015

oscillates vertically along the flame height, moving from about one-third up the flame length to two-thirds of the flame length. Similarly, the region of high ratio above it expands with the same frequency. The high ratio of about 0.7 – 0.8 expands from about the last 25% of the flame length to 50% flame length and is characterized by vortices and turbulence.

We present the total amount of radiation in the spectral bands 1 and 2 as a function of time in Fig. 7, for low (left) and high (right) oxygenation. In each case, the upper curve graphs the total power in the band 1 and the lower curve the power in the band 2. Interestingly, even though the flame appears laminar for most of its volume, we measure clear temporal variations for power in both bands. The high- oxygenation graphs on the right exhibit regular oscillatory temporal dependence. We measure about a 300-millisecond period for the band 1 and band 2 fluctuations. The curve in band 1 follows the curve in band 2 by a quarter of a oscillation period.

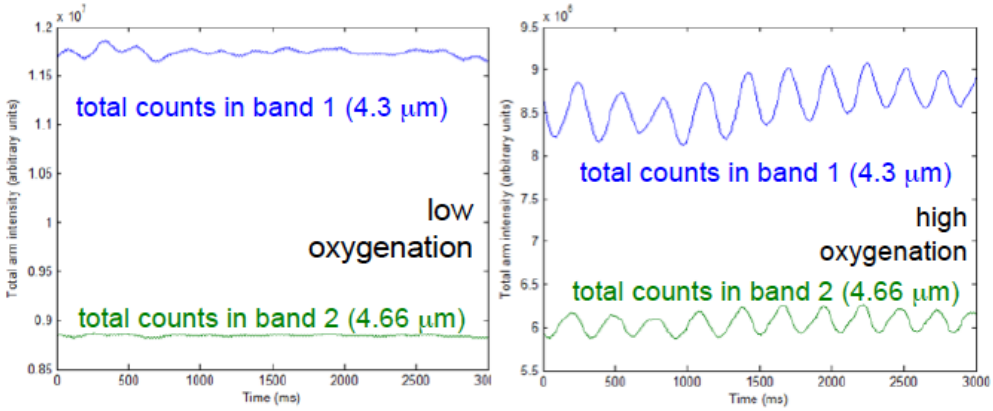

Fig. 7. Total amount of radiation in the image transmitted by filter A (4.3 μm, band 1) and filter B (4.66 μm, band 2) as a function of time, at 1,000 fps, for low- (left) and high- (right) oxygenation level. The upper and lower curves present the total power integrated over the band 1 flame image and band 2 image.

The low-oxygenation graphs on the left in Fig. 7 show some irregular, small-amplitude, mostly harmonic fluctuations. One difference between the low- and high- oxygenation is the formation and establishment of regular oscillatory behavior of radiation in 2 spectral bands.

We examine oscillatory behavior in more detail by dividing the total amount of radiation in band 1 (4.3 μm) by radiation in band 2 (4.66 μm) for each frame for both levels of oxygenation. These two graphs are displayed in Fig. 8. The intermittency of the low oxygenation case becomes more obvious upon presentation as a simple ratio of two numbers. The oscillatory behavior is better defined even though the fluctuation peaks are irregular. The average period of about 300 milliseconds may be easily discerned.

The high-oxygenation ratio graph exhibits a well-behaved oscillatory component, with a period of about 300 ms. The average value of the ratio curve appears to start increasing, potentially indicating process transition. The influx of combustion gases and the outflow of hot by-products are still being established during the initial transitory time period of about 1 second. The temporal resolution of the bispectral imager allows identification of local instabilities and permits follow-up on their progress.

#243169 Received 19 Jun 2015; revised 27 Jul 2015; accepted 29 Jul 2015; published 1 Sep 2015

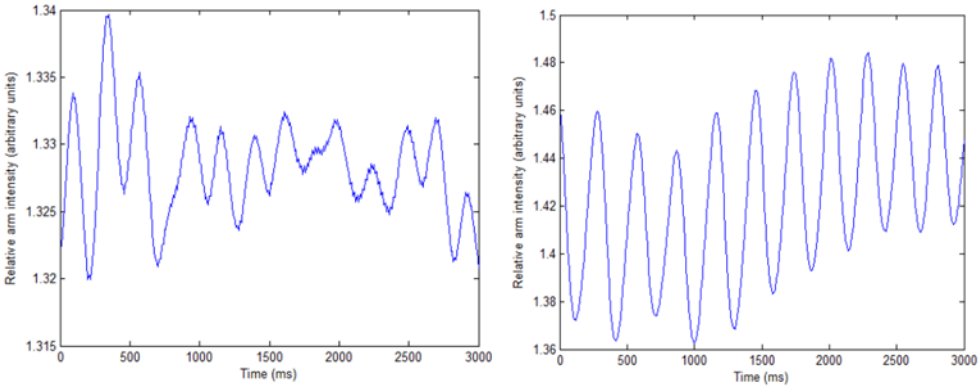

Fig. 8. The simple ratio of the total amount of radiation in band 1 (4.3 μm) over that in band 2 (4.66 μm) as a function of time at 1,000 frames per second for low- (left) and high- (right) oxygenation levels.

5. Summary and conclusions

We described the design of a bispectral imaging instrument that records two spectral, high-resolution images at rates of over 1,000 fps at mid- IR wavelengths, at spectral bands centered at 4.3 μm and 4.66 μm. The device delivers a single ratioed bispectral image every ms.

We used a Bunsen burner flame as a resolved object. We detected its evolution at 1,000 fps to demonstrate the performance of the bispectral imager. With this device, we observed two-dimensional pulsating and puffing for high and low ratio cluster of pixels. These phenomena have previously been observed in a single band: with CO_2 imaging on jet flames and H_2O imaging on hydrogen pool flames. The fluctuation in detected radiation in bands at 4.3 μm and 4.66 μm has the same frequency and includes a temporal delay of a quarter of the fluctuation period.

The present device has been designed for rapid radiation detection in two spectral regions simultaneously from the same 2-D scene. The instrument may be easily modified for other spectral bands, more spectral bands, and different conjugate points.

Acknowledgments

Authors wish to acknowledge the Concejo National de Ciencia y Tecnologia for funding this research. We thank M. K. Scholl for providing technical assistance.

#243169 Received 19 Jun 2015; revised 27 Jul 2015; accepted 29 Jul 2015; published 1 Sep 2015